

Accelerated Article Preview

Orbital Period Change of Dimorphos Due to the DART Kinetic Impact

Received: 18 November 2022

Accepted: 7 February 2023

Accelerated Article Preview

Cite this article as: Thomas, C. A. et al. Orbital Period Change of Dimorphos Due to the DART Kinetic Impact. *Nature* <https://doi.org/10.1038/s41586-023-05805-2> (2023)

Cristina A. Thomas, Shantanu P. Naidu, Peter Scheirich, Nicholas A. Moskovitz, Petr Pravec, Steven R. Chesley, Andrew S. Rivkin, David J. Osip, Tim A. Lister, Lance A. M. Benner, Marina Brozović, Carlos Contreras, Nidia Morrell, Agata Rożek, Peter Kušnírák, Kamil Hornoch, Declan Mages, Patrick A. Taylor, Andrew D. Seymour, Colin Snodgrass, Uffe G. Jørgensen, Martin Dominik, Brian Skiff, Tom Polakis, Matthew M. Knight, Tony L. Farnham, Jon D. Giorgini, Brian Rush, Julie Bellerose, Pedro Salas, William P. Armentrout, Galen Watts, Michael W. Busch, Joseph Chatelain, Edward Gomez, Sarah Greenstreet, Liz Phillips, Mariangela Bonavita, Martin J. Burgdorf, Elahe Khalouei, Penélope Longa-Peña, Markus Rabus, Sedighe Sajadian, Nancy L. Chabot, Andrew F. Cheng, William H. Ryan, Eileen V. Ryan, Carrie E. Holt & Harrison F. Agrusa

This is a PDF file of a peer-reviewed paper that has been accepted for publication. Although unedited, the content has been subjected to preliminary formatting. Nature is providing this early version of the typeset paper as a service to our authors and readers. The text and figures will undergo copyediting and a proof review before the paper is published in its final form. Please note that during the production process errors may be discovered which could affect the content, and all legal disclaimers apply.

1 **Orbital Period Change of Dimorphos Due to the DART Kinetic
2 Impact**

3
4 Cristina A. Thomas¹, Shantanu P. Naidu², Peter Scheirich³, Nicholas A. Moskovitz⁴, Petr
5 Pravec³, Steven R. Chesley², Andrew S. Rivkin⁵, David J. Osip⁶, Tim A. Lister⁷, Lance A. M.
6 Benner², Marina Brozović², Carlos Contreras⁶, Nidia Morrell⁶, Agata Rożek⁸, Peter Kušnírák³,
7 Kamil Hornoch³, Declan Mages², Patrick A. Taylor⁹, Andrew D. Seymour¹⁰, Colin Snodgrass⁸,
8 Uffe G. Jørgensen¹¹, Martin Dominik¹², Brian Skiff⁴, Tom Polakis⁴, Matthew M. Knight¹³, Tony
9 L. Farnham¹⁴, Jon D. Giorgini², Brian Rush², Julie Bellerose², Pedro Salas¹⁰, William P.
10 Armentrout¹⁰, Galen Watts¹⁰, Michael W. Busch¹⁵, Joseph Chatelain⁷, Edward Gomez^{7,16}, Sarah
11 Greenstreet¹⁷, Liz Phillips^{18,7}, Mariangela Bonavita⁸, Martin J. Burgdorf¹⁹, Elahe Khalouei²⁰,
12 Penélope Longa-Peña²¹, Markus Rabus²², Sedighe Sajadian²³, Nancy L. Chabot⁵, Andrew F.
13 Cheng⁵, William H. Ryan²⁴, Eileen V. Ryan²⁴, Carrie E. Holt¹⁴, Harrison F. Agrusa¹⁴

14
15 ¹ Northern Arizona University, Flagstaff, AZ, USA

16 ² Jet Propulsion Laboratory, California Institute of Technology, Pasadena, CA, USA

17 ³ Astronomical Institute of the Czech Academy of Sciences, Ondřejov, Czech Republic

18 ⁴ Lowell Observatory, Flagstaff, AZ, USA

19 ⁵ Johns Hopkins University Applied Physics Laboratory, Laurel, MD, USA

20 ⁶ Carnegie Institution for Science, Las Campanas Observatory, La Serena, Chile

21 ⁷ Las Cumbres Observatory, Goleta, CA, USA

22 ⁸ University of Edinburgh, Royal Observatory, Edinburgh, UK

23 ⁹ National Radio Astronomy Observatory, Charlottesville, VA, USA

24 ¹⁰ Green Bank Observatory, Green Bank, WV, USA

25 ¹¹ Niels Bohr Institute, University of Copenhagen, Copenhagen, Denmark

26 ¹² University of St Andrews, St Andrews, UK

27 ¹³ United States Naval Academy, Annapolis, MD, USA

28 ¹⁴ University of Maryland, College Park, MD, USA

29 ¹⁵ SETI Institute, Mountain View, CA, USA

30 ¹⁶ Cardiff University, Cardiff, UK

31 ¹⁷ University of Washington, Seattle, WA, USA

32 ¹⁸ University of California, Santa Barbara, CA, USA

33 ¹⁹ Universität Hamburg, Hamburg, Germany

34 ²⁰ Seoul National University, Gwanak-gu, Seoul, Korea

35 ²¹ Universidad de Antofagasta, Antofagasta, Chile

36 ²² Universidad Católica de la Santísima Concepción

37 ²³ Isfahan University of Technology, Isfahan, Iran

38 ²⁴ Magdalena Ridge Observatory, New Mexico Institute of Mining and Technology, Socorro,
39 NM, USA

40

41

42

43

44

45

46 The Double Asteroid Redirection Test (DART) spacecraft successfully performed the first
47 test of a kinetic impactor for asteroid deflection by impacting Dimorphos, the secondary of
48 near-Earth binary asteroid (65803) Didymos, and changing the orbital period of
49 Dimorphos. A change in orbital period of approximately 7 minutes was expected if the
50 incident momentum from the DART spacecraft was directly transferred to the asteroid
51 target in a perfectly inelastic collision¹, but studies of the probable impact conditions and
52 asteroid properties indicated that a considerable momentum enhancement (β) was
53 possible^{2,3}. In the years prior to impact, we used lightcurve observations to accurately
54 determine the pre-impact orbit parameters of Dimorphos with respect to Didymos^{4–6}. Here
55 we report the change in the orbital period of Dimorphos as a result of the DART kinetic
56 impact to be -33.0 ± 1.0 (3σ) minutes. Using new Earth-based lightcurve and radar
57 observations, two independent approaches determined identical values for the change in
58 the orbital period. This large orbit period change suggests that ejecta contributed a
59 significant amount of momentum to the asteroid beyond what the DART spacecraft
60 carried.

61
62 NASA's DART (Double Asteroid Redirection Test) successfully impacted Dimorphos, the
63 secondary of the near-Earth binary asteroid (65803) Didymos, on 26 September 2022 at 23:14
64 UTC. The primary objective of DART was to change the orbital period of Dimorphos around
65 Didymos to demonstrate that a kinetic impactor is a viable method of asteroid deflection^{1,7}. The
66 mission targeted the secondary asteroid in an eclipsing binary system since the experiment could
67 use a single impacting spacecraft and measure the change in the secondary's orbit through
68 ground-based observations. The Didymos system was selected as the target because it is among
69 the most accessible (low ΔV) of the near-Earth binaries, it has been extremely well
70 characterized^{4–6,8–12}, and Dimorphos is in the size range identified as relevant for deflection by a
71 kinetic impactor^{13,14}.

72
73 The DART spacecraft collided head-on into the leading hemisphere of Dimorphos in order to
74 maximize the momentum transfer and reduce the semi-major axis of the Dimorphos orbit,
75 resulting in a shorter orbital period⁷. If the incident momentum from the impacting spacecraft
76 was simply transferred to the asteroid target with no additional momentum enhancement, an
77 orbital period change for Dimorphos of roughly seven minutes was expected¹. Impact
78 simulations conducted in preparation for DART's kinetic impact test indicated that depending on
79 the material strength, impact conditions, and other properties the value of the momentum
80 enhancement factor, β , could be considerable, with predicted values as high as five² or six³ with
81 a resulting orbital period change of over 40 minutes¹⁵.

82
83 The Didymos system lightcurve is composed of three parts: the rotational lightcurve of Didymos,
84 the rotational lightcurve of Dimorphos, and the mutual events that constrain the orbital period.
85 The Didymos rotational lightcurve can be clearly distinguished because the primary contributes
86 approximately 96% of the light from the system. The Dimorphos rotational period has not been
87 resolved due to its comparatively small size, the oblate shape of Dimorphos¹⁶, and the accuracy
88 of the photometric observations necessary for such a detection. Mutual events cause a
89 measurable decrease in the total brightness of the system. We define the primary/secondary
90 occultation or eclipse based on which object is being obscured or shadowed, respectively. We
91 use the timings of the observed mutual events in the determination of the orbital period. For the

92 Didymos-Dimorphos system, mutual events occur when the Didymos-Sun or the Didymos-Earth
93 vector forms an angle less than \sim 17 degrees with the mutual orbit plane of the system. Since the
94 inclination of the mutual orbit to the heliocentric orbit of the binary system is lower than this
95 value, eclipses (mutual shadowing of the components, Figure 1) always occur. Occultations did
96 not occur during the observing period presented in this paper.
97

98 A precise determination of the Didymos system's pre-impact orbital parameters was a key goal
99 once the system was chosen as the target of DART. The initial orbit of Dimorphos was first
100 defined following the 2003 apparition when the secondary was discovered^{11,17}. Analyses of
101 lightcurve derived mutual events obtained during 2003-2022⁴ led to independent and consistent
102 orbital periods^{5,6}. The data used in the published pre-impact orbit solutions were augmented with
103 additional photometric data obtained in July 2022 to calculate the pre-impact orbit period for
104 Dimorphos (Extended Data Table 1). Both approaches determined a statistically identical pre-
105 impact orbital period of 11.92148 ± 0.00013 h (3σ).
106

107 To determine the post-impact orbital period, we obtained radar and lightcurve observations of the
108 Didymos system. Our radar observations of Didymos and Dimorphos began about 11 hours after
109 impact using the Goldstone X-band (3.5 cm, 8560 MHz) and continued for 14 dates between
110 UTC 27 September - 13 October (all subsequent dates are in UTC). We also used the Green
111 Bank Telescope to receive radar echoes in a bistatic configuration with transmissions from
112 Goldstone on 2, 6, and 9 October. We obtained echo power spectra during each of the observing
113 windows and range-Doppler images (Figure 2) on ten days centered on 4 October, when the
114 signal to noise ratios (SNRs) were the highest because Didymos was the closest to Earth. The
115 radar observations of the system are not subject to the same shadowing geometry as the
116 lightcurve photometry. Dimorphos can be seen when illuminated by radar and the system was
117 never in a radar eclipse geometry. We measured the separations between Dimorphos and
118 Didymos in the echo power spectra and the range-Doppler images. We used these measurements
119 in the determination of the orbital parameters of Dimorphos relative to Didymos. We only used
120 data in which the SNRs were strong enough to detect both Didymos and Dimorphos. The first
121 observation of Dimorphos (8σ detection), approximately 12 hours after impact, yielded the first
122 estimate of the orbital period change of -36 ± 15 minutes.
123

124 Following the DART kinetic impact, ejecta was introduced into the system¹⁸. The additional flux
125 and the variable brightness from the rapidly evolving ejecta prevented immediate observations of
126 the mutual events. Lightcurve observations began in the hours after impact and our first
127 successful detection of a mutual event was a secondary eclipse approximately 29.5 hours after
128 impact (mid-time at geocentric UT 28 September 04:50). At the time of the first mutual event
129 detection, the flux from the ejecta dominated the signal within the photometric aperture. This
130 contamination resulted in a reduction in the observed amplitude of the Didymos rotational
131 lightcurve by a factor of 3. The apparent depth of the secondary eclipse was also significantly
132 reduced compared to the predictions⁶. Pre-impact ejecta models¹⁹ suggested that it could take up
133 to several days for our ground-based lightcurve observations to detect the first mutual event due
134 to the total ejecta brightness and that the rate of change of that brightness could be comparable to
135 the expected changes in the Didymos system brightness during mutual events.
136

137 Photometric observations included in this analysis were obtained from 28 September to 10
138 October 2022 (Extended Data Table 2). This set of observations ends on 10 October because
139 subsequent observations did not have the required precision due to the bright Moon. On average
140 our data have photometric accuracy of RMS \sim 0.006 magnitudes. The exceptional quality of the
141 data included in our analysis has enabled the determination of the Dimorphos orbital period
142 change via lightcurves despite the presence of ejecta in all of our observations (Figures 3 & 4).
143 At the time of these first observations, the primary eclipses were grazing events (Figure 1),
144 which required exceptionally precise data to measure.

145
146 Two independent methods were used to model the available data for determination of the post-
147 impact orbital period: (1) we use the processes described in ref.⁶ to model the lightcurve
148 observations alone and (2) we combine the radar and mutual event timings^{5,11} plus Didymos-
149 relative astrometry of Dimorphos in optical navigation images from the DART spacecraft
150 DRACO camera²⁰. Both methods use the same ground-based photometric datasets, but have
151 independent processes for accepting individual data points and mutual events. Ellipsoidal
152 approximations of the shapes of Dimorphos and Didymos are incorporated in the calculation of
153 the orbit period of Dimorphos in both approaches and the axial ratios reported in ref.¹⁶ were
154 used for their calculation.

155
156 We determine a post-impact period of 11.372 ± 0.017 (3σ) hours with a period change of -33.0
157 ± 1.0 (3σ) minutes. Both methods provide statistically identical results for the post-impact
158 orbital period. The rotation period of Didymos is measured during the lightcurve analysis process
159 and shows no variation from its pre-impact value of 2.260 hours to an uncertainty of
160 approximately 5 seconds (3σ). The rotational lightcurve of Dimorphos has not been detected.
161 The new orbital period results in Dimorphos completing an additional full orbit every \sim 9.8 days.
162

163 The difference between the pre-impact and post-impact mutual orbit period of the Didymos-
164 Dimorphos system greatly exceeds the \sim 7 minute period change calculated for the case of a
165 simple momentum transfer with no momentum enhancement¹. Estimates of the change in orbital
166 velocity imparted to Dimorphos require modeling beyond the scope of this paper, but it is
167 evident that the ejecta from the DART impact carried a significant amount of momentum
168 compared to what the DART spacecraft itself was carrying (e.g.,²¹). To serve as a proof-of-
169 concept for the kinetic impactor technique of planetary defense, DART needed to demonstrate
170 that an asteroid could be targeted during a high-speed encounter¹⁶ and that the target's orbit
171 could be changed. DART has successfully done both.

172
173
174
175
176
177
178
179
180
181
182

References

- 183 1. Cheng, A. F. *et al.* AIDA DART asteroid deflection test: Planetary defense and science
184 objectives. *Planet. Space Sci.* **157**, 104–115 (2018).
- 185 2. Stickle, A. M. *et al.* Effects of Impact and Target Parameters on the Results of a Kinetic
186 Impactor: Predictions for the Double Asteroid Redirection Test (DART) Mission. *Planet. Sci.
187 J.* **3**, 248 (2022).
- 188 3. Raducan, S. D. & Jutzi, M. Global-scale Reshaping and Resurfacing of Asteroids by Small-
189 scale Impacts, with Applications to the DART and Hera Missions. *Planet. Sci. J.* **3**, 128
190 (2022).
- 191 4. Pravec, P. *et al.* Photometric Observations of the Binary Near-Earth Asteroid (65803)
192 Didymos in 2015–2021 Prior to DART Impact. *Planet. Sci. J.* **3**, 175 (2022).
- 193 5. Naidu, S. P. *et al.* Anticipating the DART Impact: Orbit Estimation of Dimorphos Using a
194 Simplified Model. *Planet. Sci. J.* **3**, 234 (2022).
- 195 6. Scheirich, P. & Pravec, P. Preimpact Mutual Orbit of the DART Target Binary Asteroid
196 (65803) Didymos Derived from Observations of Mutual Events in 2003–2021. *Planet. Sci. J.*
197 **3**, 163 (2022).
- 198 7. Rivkin, A. S. *et al.* The Double Asteroid Redirection Test (DART): Planetary Defense
199 Investigations and Requirements. *Planet. Sci. J.* **2**, 173 (2021).
- 200 8. Fang, J. & Margot J.-L. Near-Earth Binaries and Triples: Origin and Evolution of Spin-Orbital
201 Properties. *Astron. J.*, **143**, 24 (2012).
- 202 9. de León, J., Licandro, J., Duffard, R. & Serra-Ricart, M. Spectral analysis and mineralogical
203 characterization of 11 olivine–pyroxene rich NEAs. *Adv. Space Res.* **37**, 178–183 (2006).
- 204 10. Dunn, T. L., Burbine, T. H., Bottke, W. F. & Clark, J. P. Mineralogies and source regions
205 of near-Earth asteroids. *Icarus* **222**, 273–282 (2013).

- 206 11.Naidu, S. P. *et al.* Radar observations and a physical model of binary near-Earth asteroid
207 65803 Didymos, target of the DART mission. *Icarus* **348**, 113777 (2020).
- 208 12.Ieva, S. *et al.* Spectral Rotational Characterization of the Didymos System prior to the DART
209 Impact*. *Planet. Sci. J.* **3**, 183 (2022).
- 210 13.*Defending Planet Earth: Near-Earth Object Surveys and Hazard Mitigation Strategies*. 12842
211 (National Academies Press, 2010). doi:10.17226/12842.
- 212 14.Interagency Working Group for Detecting and Mitigating the Impact of Earth-bound Near-
213 Earth Objects. National Near-Earth Object Preparedness Strategy and Action Plan. (2018).
- 214 15.Meyer, A. J. *et al.* Libration-induced Orbit Period Variations Following the DART Impact.
215 *Planet. Sci. J.* **2**, 242 (2021).
- 216 16.Daly, R. T. *et al.* DART: An Autonomous Kinetic Impact into a Near-Earth Asteroid for
217 Planetary Defense. *Nature (this issue)*, (2022).
- 218 17.Pravec, P. *et al.* Photometric survey of binary near-Earth asteroids. *Icarus* **181**, 63–93 (2006).
- 219 18.Li, J.-Y. *et al.* Ejecta Evolution of the First Human-Activated Asteroid Produced by DART
220 Impact. *Nature (this issue)*, (2022).
- 221 19.Fahnestock, E. G. *et al.* Pre-encounter Predictions of DART Impact Ejecta Behavior and
222 Observability. *Planet. Sci. J.* **3**, 206 (2022).
- 223 20.Fletcher, Z. J. *et al.* Didymos Reconnaissance and Asteroid Camera for OpNav (DRACO):
224 design, fabrication, test, and operation. in *Space Telescopes and Instrumentation 2022:*
225 *Optical, Infrared, and Millimeter Wave* (eds. Coyle, L. E., Perrin, M. D. & Matsuura, S.) 11
226 (SPIE, 2022). doi:10.11117/12.2627873.
- 227 21.Statler, T. S. *et al.* After DART: Using the First Full-scale Test of a Kinetic Impactor to
228 Inform a Future Planetary Defense Mission. *Planet. Sci. J.* **3**, 244 (2022).

229 **Methods**

230
231 The models incorporated three types of observations of the Didymos-Dimorphos system:
232 photometric lightcurves, radar, and Didymos-relative astrometry from DART's DRACO
233 camera²⁰. We determined the post-impact orbital period using two separate models (ref. 6,
234 hereafter SP22, and ^{5,11}; hereafter N22+). Both approaches use the same sets of pre and post-
235 impact lightcurves (Extended Data Tables 1 & 2). The SP22 approach models the lightcurve
236 observations to determine the properties of the orbit. The N22+ approach incorporates Didymos-
237 relative astrometry from DRACO optical navigation images to update the orbital parameters of
238 the pre-impact orbit and includes lightcurve mutual event timings and radar observations for the
239 post-impact solution (Extended Data Tables 3-7).

240
241 **Photometric Lightcurve Data & Reductions**

242
243 Previous observations of the Didymos system⁴ demonstrated the need for requirements on the
244 photometry used in the analysis. We define our data quality requirement as an RMS < 0.01
245 magnitudes, where the RMS value refers to the consistency over the nightly run and results in a
246 minimum signal-to-noise (SNR) on the individual exposures of ~100. For an accurate
247 decomposition of the lightcurve, we require adequate coverage of the primary lightcurve outside
248 of mutual events. We prefer two complete rotation periods of the primary ($P_{\text{rot}}=2.26$ hr) outside
249 of the events and estimate this requirement as 6 hours of continuous observation. The
250 observations can be split between multiple stations. Four observatories contributed data that met
251 the photometric requirements to the lightcurve dataset for the orbital period change (Extended
252 Data Table 2): Las Campanas Observatory 1-m Swope Telescope, the Las Cumbres Observatory
253 global telescope network 1-m telescopes, the Danish 1.54-m telescope at the European Southern
254 Observatory's La Silla site, and the Lowell Observatory 1.1-m Hall telescope.

255
256 The Las Campanas Observatory Swope 1-m telescope is located in the Atacama Desert, Chile²².
257 The Swope 4K CCD is a visible-wavelength, direct-imaging CCD with a 29.7 x 29.8 arc-minute
258 field of view. Swope observations were taken in the Sloan-r' filter and used sidereal tracking
259 with 1 or 2 sky pointings each night. Instrumental aperture photometry was performed on every
260 frame using the python package SEP²³. We use the astroquery Python package to query Vizier²⁴
261 and Horizon²⁵ databases to identify *Gaia* stars and to obtain the coordinates of the asteroid for
262 the given date of the images, respectively, and the gaiaxy Python package, to request and
263 download synthetic photometry of *Gaia* stars²⁶ in Sloan-r band when available. The Swope data
264 show discrepancies in the photometry (as seen in Figure 2) at the ~0.01-0.02 mag level. There
265 are no issues on the timing of the events, which are the key drivers for the derivation of the new
266 orbit period. Additional reductions of this data with optimized apertures will be used to address
267 these discrepancies.

268
269 The Las Cumbres Observatory global telescope (LCOGT) network²⁷ consists of telescopes at
270 seven sites around the world, operated robotically using dynamical scheduling software²⁸. We
271 used the 1-m telescopes at the South Africa and Chile nodes with the telescopes tracking at half
272 of the ephemeris rates. These observations were scheduled and reduced using the NEOexchange
273 Target and Observation Manager and data reduction pipeline²⁹. Images were pre-processed using

274 the Python-based BANZAI pipeline³⁰. Astrometry and photometry was performed using the
275 Python-based NEOexchange pipeline²⁹. The LCOGT data was primarily obtained in
276 PanSTARRS-w band (equivalent to a broad $g + r + i$ band) and was calibrated to the *Gaia*-DR2³¹
277 using calviacat³², with the w band treated as an r band. Calibration stars were constrained to have
278 “solar-like” colors.

280 The Danish 1.54-m telescope is located at the European Southern Observatory’s La Silla site in
281 Chile. Observations were performed by the MiNDSTEp (Microlensing Network for the
282 Detection of Small Terrestrial Exoplanets) consortium. The Danish Faint Object Spectrograph
283 and Camera (DFOSC) instrument, with field of view 13.7' x 13.7', was used in imaging mode.
284 Images were taken with the Bessell R filter using sidereal tracking. Data reduction used a custom
285 Python pipeline, including alignment of frames using Astrometry.net tools³³. Relative
286 photometry was calibrated using the procedure outlined in ref. ³⁴ using the calviacat³² package
287 and the *Gaia* DR3 star catalog, with conversion to SDSS- r band magnitudes assuming a color of
288 ($g-r$)=0.52 for Didymos^{4,35}.

290 The Lowell 1.1-m Hall telescope, located on Anderson Mesa south of Flagstaff, Arizona, is
291 equipped with a 4k x 4k CCD that images a 25 arcmin square field. The telescope was tracked at
292 half of the ephemeris rate. Exposures were taken with a broad VR -band filter. Photometric
293 calibration was based on field star magnitudes from the PanSTARRS catalog. Only stars with
294 high signal-to-noise (>100) and solar-like colors were used for calibration. For the 2022-10-02
295 data, the photometry was measured using the Canopus software package. For the 2022-10-05
296 data, the photometry was measured using the PhotometryPipeline³⁶.

298 We added lightcurve observations from three telescopes (Table 1) to augment the pre-impact
299 lightcurve solutions published in ref. ⁶ and ⁵: the 6.5-m Magellan Baade telescope, the SOAR
300 (Southern Astrophysical Research) 4.1-m telescope, and the 4.3-m Lowell Discovery Telescope.
301 Both of the updated models confirmed the previous solutions.

303 Lightcurve Decomposition

305 To model the photometric data of the binary asteroid system, we follow the decomposition
306 methods defined in ref. ^{17,37} and discussed in ref. ⁴. Outside of mutual events, the largest signal in
307 the Didymos system lightcurve is the flux of the primary which can be represented by the
308 following Fourier series:

$$310 \quad F_1(t) = C_1 + \sum_{k=1}^{m_1} \left[C_{1k} \cos \frac{2\pi k}{P_1} (t - t_0) + S_{1k} \sin \frac{2\pi k}{P_1} (t - t_0) \right]$$

313 $F_1(t)$ is the flux of the primary, Didymos, at time t , C_1 is the mean flux of the primary, C_{1k} and
314 S_{1k} are the Fourier coefficients, P_1 is the lightcurve rotational period of Didymos, t_0 is the zero-
315 point time, and m_1 is the maximum significant order. By using this mathematical representation
316 for the system, we assume that Didymos is in principal axis rotation, that mutual illumination
317 between the objects is negligible, and that the rotational lightcurve does not change with time.

318 The lightcurve data is corrected to constant geocentric and heliocentric distances and a consistent
319 solar phase angle. We connect data from different telescopes by scaling them in relative
320 magnitude compared to each other, which has no impact on the timing of the mutual events.

321
322 We use observations taken outside of mutual events to fit the rotational lightcurve of Didymos.
323 The rapidly changing Earth-Didymos-Sun geometry during this period of Didymos' close
324 approach to Earth causes observable changes in the primary rotational lightcurve. For our
325 previous work⁴, we were able to combine data on the timescales of days to weeks. For this
326 dataset, separate decompositions are done for each Julian Day (JD). We correct for the overall
327 fading of the ejecta for each dataset by fitting a linear flux trend before performing the lightcurve
328 decomposition.
329

330 **Radar Observations**

331
332 We observed Didymos and Dimorphos using the Goldstone X-band radar (3.5 cm, 8560 MHz)
333 on the 70-m DSS-14 telescope on 14 dates between 27 September - 13 October 2022. On 2, 6,
334 and 9 October, we also used the 100-m Green Bank Telescope to receive radar echoes in a
335 bistatic configuration with transmissions from Goldstone. Typical transmitter power was 430
336 kW. We obtained echo power spectra during each of the observing windows and range-Doppler
337 images on several days centered on 4 October when the signal to noise ratios (SNRs) were the
338 highest. Didymos was clearly detected in all of the data ($> 3\sigma$) and its maximum bandwidth
339 varied from 22 Hz on 27 September, when the subradar latitude was -50 degrees, to 34 Hz on 13
340 October, when its subradar latitude was -32 degrees (based on the pole direction estimated by
341 ref. ¹¹).
342

343 Detecting Dimorphos was challenging and required experimenting with setups having different
344 frequency resolutions, range resolutions, and integration times. This process was a trade-off
345 between obtaining longer integrations with sufficiently high SNRs to detect Dimorphos versus
346 reducing the smearing caused by the orbital motion during the integration. We found that the
347 echo from Dimorphos was most consistently visible at resolutions of 1 Hz in the echo power
348 spectra and at 0.5 Hz in the images. Due to the 11.9 h rotation period, a diameter of ~160 meters,
349 and a subradar latitude of -50 to -30 deg¹¹, the echo from Dimorphos was expected to have a
350 bandwidth of about 1 Hz¹¹, so the data do not resolve Dimorphos in frequency but maximize the
351 SNRs by nearly matching the bandwidth. The contribution of self-noise in the echo power
352 spectra is negligible and does not affect the SNRs significantly. We attempted imaging with time
353 delay resolutions of 0.5 μ s and 1 μ s (corresponding to range resolutions of 75 m and 150 m), and
354 found that the 0.5 μ s setup yielded more consistent detections. We experimented with summing
355 data spanning a range of time intervals and found that the echo from Dimorphos was not clearly
356 visible in all the data on any given day. It became more difficult to detect Dimorphos after 4
357 October as the distance to Didymos increased and the SNRs correspondingly decreased. Figure 2
358 shows range-Doppler images and Extended Data Figure 5 shows selected echo power spectra in
359 which the echo from Dimorphos was seen.
360

361 We measured the separations between Dimorphos and Didymos in the echo power spectra and
362 range-Doppler images and used these measurements in the estimation of the orbital parameters
363 of Dimorphos relative to Didymos. The separations in Doppler frequency and range between

364 Didymos and Dimorphos relate to the relative velocity and distance along the observer's line of
365 sight due to their mutual orbit about each other. We used only data in which both Didymos and
366 Dimorphos were clearly visible for making these measurements. The echo power spectra were
367 processed so that hypothetical echoes from the Didymos system barycenter appear at 0 Hz³⁸.
368 Because the reflex motion of Didymos about the system barycenter is < 10 m (0.08 Hz)¹¹, we
369 assumed that the Didymos center of mass (COM) is at 0 Hz so that the Doppler frequency of
370 Dimorphos represents the relative Doppler shift. The echo from Dimorphos is unresolved so we
371 assumed that its COM was located in the Doppler bin that contained the strongest spike due to
372 the echo from Dimorphos. We assigned uncertainties of ± 2 Hz to the Doppler separation
373 measurements to take into account the uncertainties due to the frequency resolution of the spectra
374 (1 Hz), the ephemeris errors in the location of the system barycenter (0.24 Hz, 3σ), and the reflex
375 motion of Didymos about the system barycenter (< 0.1 Hz). Consequently, the principal source
376 of uncertainty in measurements of the range-Doppler separations are the Doppler frequencies of
377 Dimorphos.
378

379 Due to the low SNRs, the COM of Didymos is hard to locate in the range-Doppler images, so we
380 assumed it is located 375 m (5 range pixels at 75 m/pixel) behind the leading edge, which is the
381 brightest part of the echo and easiest to see. This distance equals the equatorial radius reported
382 from the 3D shape model obtained by ref. ¹¹ and is consistent with preliminary estimates from
383 the DART spacecraft images reported by ref. ¹⁶. The echo from Dimorphos extended over one to
384 three range rows and we assumed that its COM is in the trailing row. We assigned uncertainties
385 of 150 m (two range rows) to the range separation measurements. Tables 5 and 6 show the range
386 and Doppler frequency of Dimorphos relative to Didymos that were used in the orbit
387 determination. We estimated 8 range measurements on 9 October (when reception at Green Bank
388 facilitated detecting echoes from Dimorphos), far more than on any other day, so we inflated
389 their uncertainties by a factor of 3 in order to mitigate the effects of correlated errors.
390

391 Didymos-Relative Optical Astrometry from DRACO images

392

393 We measured the positions of Dimorphos relative to Didymos in 16 DRACO images taken in the
394 minutes prior to impact on 26 September 2022 between 23:10:58.235 and 23:12:39.336 UTC to
395 use in the orbit estimation process. At the time these measurements were made, no shape models
396 estimated from spacecraft images were available to fit to the partially illuminated figures of the
397 two bodies, so we measured the intersections of the limbs with the relative position vectors.
398 These measurements were differenced to estimate the limb-to-limb positions of Dimorphos
399 relative to Didymos. These positions were mapped from image coordinates into Right Ascension
400 (RA) and Declination (DEC) using the camera model and the GNC (Guidance, Navigation, and
401 Control) spacecraft attitude knowledge. Measurement uncertainties of 1.13×10^{-3} degrees (3σ)
402 were derived by repeating this process and comparing the different observations. We assumed
403 the equatorial extents of Didymos and Dimorphos to be 425 m and 88 m respectively and added
404 an angular distance corresponding to $425 - 88 = 337$ m (± 20 m 1σ) uncertainty) in the direction
405 of the limb-to-limb separations to estimate the distances between the COMs. Since the
406 measurements covered a very short time span, we de-weighted the uncertainties by $4x$ ($\sqrt{16}$) to
407 mitigate effects of correlated measurement errors. We de-weighted the DEC measurements by an
408 additional factor of two because they are clearly noisier than the RA measurements. Extended
409 Data Table 7 lists the observations and uncertainties.
410

411 **Orbital Period Determination Via Lightcurves (SP22 Method)**

412
413 The ref.⁶ numerical model of the Didymos system was developed using the techniques described
414 in ref.^{39–41}. Didymos and Dimorphos are represented by ellipsoids with axial ratios of
415 $a_1/c_1=b_1/c_1=1.37$, $a_2/c_2=1.53$, $b_2/c_2=1.50^{16}$. The motion of the two bodies is assumed to be
416 Keplerian. The post-impact system was analyzed with no *a priori* assumption on the new binary
417 orbital period. The lightcurve data from 28 & 29 September showed that parts of the data were
418 attenuated with respect to the primary's rotational lightcurve. Those sections of the data were
419 iteratively masked until all of the data points in the mutual events were identified and the
420 lightcurve decomposition was complete. The first mutual event (0.03 magnitudes deep) was
421 determined to be a secondary eclipse since the system geometry predicted very shallow or absent
422 primary events.

423 We adapted the method from ref.⁶ to estimate the uncertainty of the post-impact period. When
424 stepping the period over a suitable interval we computed normalized χ^2 for each step. We
425 determined its 3σ uncertainty as an interval in which χ^2 is below a certain limit. The adopted
426 limiting p-value corresponds to the probability that the χ^2 exceeds a particular value only by
427 chance equal to 0.27%. At each step of the period scanning, the mean anomaly of Dimorphos at
428 the epoch of the impact was also scanned within its 3σ uncertainty interval that was determined
429 by ref.⁶ and that we have updated using the additional data taken in July 2022. The SP22 pre-
430 impact period was 11.921478 ± 0.000123 (3σ) hours.

431
432 The SP22 model determines a post-impact period of 11.372 ± 0.017 (3σ) hours corresponding to
433 an orbit period change of -33.0 ± 1.0 (3σ) minutes.

434 **Orbital Period Determination via Radar and Lightcurves (N22+ Method)**

435
436 The lightcurve analysis method described in ref.⁵ is a less complicated approach compared to the
437 methods presented in ref.⁶. However, it has the advantage of combining information from
438 different data types such as radar, relative optical astrometry from DRACO images, and
439 lightcurve mutual events. The pre-impact orbital period using the N22+ approach was 11.92148
440 ± 0.00013 (3σ) hours.

441 Lightcurve decomposition was done independently from the SP22 process and required
442 identifying mutual events. The first identified post-impact mutual event was on UTC 28
443 September 2022. We expected that the head-on impact would decrease the orbital period
444 compared to the pre-impact solution and expected an event with a length of approximately 1
445 hour. To identify the mutual event, we tested a range of orbit periods from 11-12 hours in time
446 steps of 0.1 hours with a best match of 11.4 hours. Subsequent observations helped refine the
447 initial estimate.

448
449 For each mutual event there are four contact times: when the event begins and flux decreases
450 (T_1), when flux reaches a minimum (T_2), when the flux begins to increase (T_3), and when the
451 event ends and the flux returns to the baseline (T_4). We use times $T_{1.5}$ and $T_{3.5}$ in the orbit
452 determination. These times are when the flux is at half the total drop in flux during the event (Fig
453 1 in ref.⁵). We use 1σ uncertainties of $(T_{1.5} - T_1)/2$ and $(T_4 - T_{3.5})/2$ for $T_{1.5}$ and $T_{3.5}$, respectively.

457 We used a least-squares approach, as described in ref.⁵, for estimating the orbital parameters of
458 Dimorphos relative to Didymos. Prior to the DART impact, Dimorphos is assumed to be a point
459 mass on a modified Keplerian orbit around Didymos with an additional term for modeling the
460 drift in mean motion due to nongravitational effects such as the Binary YORP effect and tidal
461 dissipation. The post-impact orbit was assumed to be Keplerian, since the data-arc length is too
462 short to detect a drift in mean motion. We used Δn to capture the change in mean motion due to
463 the DART impact. The mean anomaly, M , and mean motion, n , of Dimorphos at time, t , are
464 given by:

465
$$M(t) = M_0 + n_0(t - t_0) + \frac{1}{2}\dot{n}(t - t_0)^2 \text{ for } t < t_{imp}$$

466
$$M(t) = M_{imp} + (n_{imp} + \Delta n)(t - t_{imp}) \text{ for } t > t_{imp}$$

467
$$n(t) = n_0 + \dot{n}(t - t_0) \text{ for } t < t_{imp}$$

468
$$n(t) = n_{imp} + \Delta n \text{ for } t > t_{imp}$$

469 Where t_{imp} is time of the DART impact, M_0 and n_0 are the mean anomaly and mean motion at t_0 ,
470 \dot{n} is the linear drift in mean motion due to nongravitational effects, and M_{imp} and n_{imp} are the
471 mean anomaly and mean motion at impact.

472 We used differential corrections as described in ref.⁵ for estimating the orbital parameters M_0 ,
473 n_0 , \dot{n} , Δn , the pre-impact semimajor axis (a), and the orbit pole longitude (λ) and latitude (β).
474 This requires calculating a computed value corresponding to each observation using a model. We
475 used three kinds of observations: lightcurve mutual event times, radar range and Doppler
476 measurements of Dimorphos relative to Didymos, and the separation of Dimorphos from
477 Didymos as seen in spatially-resolved DRACO images. The modeling of the first two
478 observables is described in ref.⁵. In order to model the separation of Dimorphos from Didymos
479 in DRACO images, we used SPICE⁴² to subtract the RA and DEC of the COM of Didymos from
480 those of the COM of Dimorphos as seen from the DART spacecraft.

481 The N22+ approach results in a post-impact period of 11.371 ± 0.016 (3σ) hours and an orbit
482 period change of -33.0 ± 1.0 (3σ) minutes. The best fit orbit parameters are presented in Table 3.
483

484 Methods References

- 485
- 486 22.Bowen, I. S. & Vaughan, A. H. The Optical Design of the 40-in Telescope and of the Irene
487 DuPont Telescope at Las Campanas Observatory, Chile. *Appl. Opt.* **12**, 1430 (1973).
- 488 23.Barbary, K. SEP: Source Extractor as a library. *J. Open Source Softw.* **1**, 58 (2016).
- 489 24. Ochsenbein, F., Bauer, P., & Marcout, J. The VizieR database of astronomical catalogues.
490

- 491 *Astron. Astrophys. Suppl. Ser.* **143**, 23 (2000).
- 492
- 493 25.Giorgini, J. D. *et al.* JPL's On-Line Solar System Data Service. in *AAS/Division for Planetary*
- 494 *Sciences Meeting Abstracts #28* vol. 28 25.04 (1996).
- 495 26. Montegriffo, P., et al. Gaia Data Release 3: The Galaxy in your preferred colours. Synthetic
- 496
- 497 photometry from Gaia low-resolution spectra. *arXiv preprint arXiv:2206.06215* (2022).
- 498
- 499 27.Brown, T. M. *et al.* Las Cumbres Observatory Global Telescope Network. *Publ. Astron. Soc.*
- 500 *Pac.* **125**, 1031–1055 (2013).
- 501 28.Saunders, E. S., Lampoudi, S., Lister, T. A., Norbury, M. & Walker, Z. Novel scheduling
- 502 approaches in the era of multi-telescope networks. in (eds. Peck, A. B., Benn, C. R. &
- 503 Seaman, R. L.) 91490E (2014). doi:10.1111/12.2056642.
- 504 29.Lister, T. A. *et al.* NEOExchange - an online portal for NEO and Solar System science. *Icarus*
- 505 **364**, 114387 (2021).
- 506 30.McCully, C. *et al.* Real-time processing of the imaging data from the network of Las
- 507 Cumbres Observatory Telescopes using BANZAI. in *Software and Cyberinfrastructure for*
- 508 *Astronomy V* (eds. Guzman, J. C. & Ibsen, J.) 22 (SPIE, 2018). doi:10.1111/12.2314340.
- 509 31.Gaia Collaboration *et al.* *Gaia* Data Release 2: Summary of the contents and survey
- 510 properties. *Astron. Astrophys.* **616**, A1 (2018).
- 511 32.Kelley, M. & Lister, T. mkelley/calviacat: v1.3.0. (2022) doi:10.5281/ZENODO.7019180.
- 512 33.Lang, D., Hogg, D. W., Mierle, K., Blanton, M. & Roweis, S. ASTROMETRY.NET: BLIND
- 513 ASTROMETRIC CALIBRATION OF ARBITRARY ASTRONOMICAL IMAGES. *Astron.*
- 514 *J.* **139**, 1782–1800 (2010).
- 515 34.Kokotanekova, R. *et al.* Rotation of cometary nuclei: new light curves and an update of the
- 516 ensemble properties of Jupiter-family comets. *Mon. Not. R. Astron. Soc.* **471**, 2974–3007

- 517 (2017).
- 518 35. Gaia Collaboration *et al.* Gaia Data Release 3: Summary of the content and survey
519 properties. (2022) doi:10.48550/ARXIV.2208.00211.
- 520 36. Mommert, M. PHOTOMETRYPIPELINE: An automated pipeline for calibrated photometry.
521 *Astron. Comput.* **18**, 47–53 (2017).
- 522 37. Pravec, P. *et al.* Two-Period Lightcurves of 1996 FG3, 1998 PG, and (5407) 1992 AX: One
523 Probable and Two Possible Binary Asteroids. *Icarus* **146**, 190–203 (2000).
- 524 38. Ostro, S. J. Planetary radar astronomy. *Rev. Mod. Phys.* **65**, 1235–1279 (1993).
- 525 39. Scheirich, P. & Pravec, P. Modeling of lightcurves of binary asteroids. *Icarus* **200**, 531–547
526 (2009).
- 527 40. Scheirich, P. *et al.* The binary near-Earth Asteroid (175706) 1996 FG3 — An observational
528 constraint on its orbital evolution. *Icarus* **245**, 56–63 (2015).
- 529 41. Scheirich, P. *et al.* A satellite orbit drift in binary near-Earth asteroids (66391) 1999 KW4 and
530 (88710) 2001 SL9 - Indication of the BYORP effect. *Icarus* **360**, 114321 (2021).
- 531 42. Acton, C., Bachman, N., Semenov, B. & Wright, E. A look towards the future in the handling
532 of space science mission geometry. *Planet. Space Sci.* **150**, 9–12 (2018).
- 533 43. Margot, J.-L., Pravec, P., Taylor, P., Carry, B. & Jacobson, S. Asteroid Systems: Binaries,
534 Triples, and Pairs. in *Asteroids IV* (eds. Michel, P., DeMeo, F. E. & Bottke, W. F.) (University
535 of Arizona Press, 2015). doi:10.2458/azu_uapress_9780816532131-ch019.

536
537
538
539
540
541
542
543

544
545

546 **Data Availability**

547
548 The lightcurves and radar data used in this analysis of the orbital period are available in the
549 JHU/APL Data archive at: <https://lib.jhuapl.edu/papers/orbital-period-change-of-dimorphos-due-to-the-dart/>. The DRACO images can be found in an archive associated with the Daly et al. paper
550 (<https://lib.jhuapl.edu/papers/dart-an-autonomous-kinetic-impact-into-a-near-eart/>).
551

552
553 In addition, all observations from Las Campanas Observatory, Las Cumbres Observatory global
554 telescope (LCOGT) network, and the Lowell Discovery Telescope will be publicly archived at
555 the Planetary Data System Small Bodies Node with the DART mission data by October 2023.
556 The radar datasets will be separately archived at the Planetary Data System.

557 **Code Availability**

558
559 The algorithms used here were published in Scheirich & Pravec (2022) and Naidu et al. (2022).
560

561 **Acknowledgements**

562
563 This work was supported by the DART mission, NASA Contract No. 80MSFC20D0004. Part of
564 this research was carried out at the Jet Propulsion Laboratory, California Institute of Technology,
565 under a contract with the National Aeronautics and Space Administration. The work by P.S. and
566 P.P. was supported by the Grant Agency of the Czech Republic, grant 20-04431S. They
567 appreciate access to computing and storage facilities owned by parties and projects contributing
568 to the National Grid Infrastructure MetaCentrum provided under the program "Projects of Large
569 Research, Development, and Innovations Infrastructures" (CESNET LM2015042) and the
570 CERIT Scientific Cloud LM2015085. The Green Bank Observatory is a facility of the National
571 Science Foundation operated under cooperative agreement by Associated Universities, Inc.
572 Observations at the Danish 1.54m telescope were supported, in part, by the European Union
573 H2020-SPACE-2018-2020 research and innovation programme under grant agreement No.
574 870403 (NEOROCKS). This work makes use of observations from the Las Cumbres
575 Observatory global telescope network. This paper includes data gathered with the 6.5 meter
576 Magellan Telescopes located at Las Campanas Observatory, Chile. Based on observations
577 obtained at the Southern Astrophysical Research (SOAR) telescope, which is a joint project of
578 the Ministério da Ciência, Tecnologia e Inovações do Brasil (MCTI/LNA), the US National
579 Science Foundation's NOIRLab, the University of North Carolina at Chapel Hill (UNC), and
580 Michigan State University (MSU). These results made use of the Lowell Discovery Telescope
581 (LDT) at Lowell Observatory. Lowell is a private, non-profit institution dedicated to
582 astrophysical research and public appreciation of astronomy and operates the LDT in partnership
583 with Boston University, the University of Maryland, the University of Toledo, Northern Arizona

584 University and Yale University. U.G.J. acknowledges funding from the Novo Nordisk
585 Foundation Interdisciplinary Synergy Programme grant no. NNF19OC0057374, and from the
586 European Union H2020-MSCA-ITN-2019 grant no. 860470 (CHAMELEON). E.K. is supported
587 by the National Research Foundation of Korea 2021M3F7A1082056. P.L.P. was partly funded
588 by "Programa de Iniciación en Investigación-Universidad de Antofagasta. INI-17-03".

589 **Author Contributions**

590
591 C.A.T. is the lead of the DART mission's Observations Working Group. She coordinated
592 observations, led the paper writing, and participated in the observing. S.P.N and P.S performed
593 the independent modeling efforts to determine the post-impact period and period change. N.A.M.
594 and P.P. accepted lightcurve data based on the requirements and performed the decompositions.
595 S.R.C. supported orbit estimation of Dimorphos. A.S.R., N.L.C., and A.F.C. lead the DART
596 Investigation Team, contributed to the writing and revision of this paper, and coordinated inputs
597 across the DART Investigation Team. D.J.O., C.C., N.M. planned, executed, and reduced the
598 data from Las Campanas Observatory's Swope telescope. T.A.L. led the data collection from the
599 Las Cumbres Observatory global telescope network. L.A.M.B. and M.B. assisted with proposal
600 writing, observing, and data processing for the radar observations. A.R., P.K., and K.H.
601 performed data reduction and photometry for the Danish telescope data set. D.M. and B.R.
602 measured the positions of in the OPNAV images. P.A.T., A.D.S., P.S., W.P.A., and G.W. helped
603 with the Green Bank Observatory observations. M.W.B. assisted with the proposal for Green
604 Bank Observatory. C.S., U.G.J., and M.D. planned and coordinated observations at the Danish
605 telescope. B.S. and T.P. performed the observations and reductions for the Lowell Hall
606 telescope. M.M.K., T.L.F., and C.E.H. performed the observations for the Lowell Discovery
607 Telescope. J.D.G. and M.B. assisted with the planning of the radar observations. J.B. generated
608 the spacecraft SPK that was used in the OPNAV treatment. J.C., E.G., S.G., and L.P. guilt the
609 portal and pipeline for scheduling and reducing the LCOGT data. M.B., M.J.B., E.K., P.L.-P.,
610 M.R., and S.S. performed observations at the Danish Telescope. W.H.R. and E.V.R assisted with
611 planning the observing effort. H.F.A. provided comments on the manuscript and performed the
612 formatting.
613
614

615 **Competing Interests**

616
617 The authors declare no competing interests.
618

619 **Additional Information**

620
621 Correspondence should be addressed to Dr. Cristina Thomas (cristina.thomas@nau.edu)
622
623

624 **Legend**

625 **Figure 1:**

626 **Post-impact Didymos system geometry.** We determine the new orbital period of Dimorphos
627 using the times of mutual events when a measurable decrease in the system brightness occurs
628 due to an eclipse or occultation. Due to the geometry of the Didymos system during this time
629 period, our lightcurve observations include primary eclipses (left), time outside mutual events
630 (center), and secondary eclipses (right). These diagrams simulate the view of the system from
631 Earth on 10 October 06:09 (primary eclipse), 10 October 08:47 (outside events), 10 October
632 12:06 (secondary eclipse) in geocentric UTC. The primary eclipses observed throughout our
633 post-impact dataset are grazing, which resulted in a subtle decrease in system brightness (Figure
634 3). During the secondary eclipse, Dimorphos is completely shadowed.
635

636 **Figure 2:**

637 **Radar range-Doppler images of the post-impact Didymos system.** Radar range-Doppler
638 images obtained on October 4 using Goldstone and October 9 using Goldstone to transmit and
639 the Green Bank Telescope to receive. Within each image, distance from Earth increases from top
640 to bottom and Doppler frequency increases to the right, so rotation and orbital motion are
641 counterclockwise. Each image was integrated for 20 minutes, with 10 minutes of overlap
642 between successive images. Images have resolutions of 75 m x 0.5 Hz. The broader echo is from
643 Didymos and the smaller, fainter echo shown using arrows is from Dimorphos. Open circles
644 show Dimorphos positions predicted by the pre-impact orbit. The yellow ellipses show the
645 trajectory of Dimorphos. Prediction uncertainties are smaller than the image resolution. On
646 October 4, the ellipse spans -870 m to +870 m along the y-axis and -7 Hz to +7 Hz along the x-
647 axis, corresponding to line of sight velocity of -12 cm/s to +12 cm/s. On October 9, the ellipse
648 spans -980 m to +980 m along the y-axis and -8 Hz to +8 Hz along the x-axis, corresponding to
649 line of sight velocity of -14 cm/s to +14 cm/s. The physical extents of the ellipse vary due to the
650 viewing geometry.
651

652 **Figure 3:**

653 **Post-impact photometric lightcurve of the Didymos system.** Measured photometry from UTC
654 2 October 2022 phase folded to the 2.26 h rotation period of Didymos (top), and the extracted
655 mutual events (= observed data - 9th order Fourier fit to Didymos' rotation) phase folded to the
656 new orbit period of Dimorphos (bottom). These lightcurves, collected from five different
657 telescopes, show photometric accuracy similar to all the lightcurve data sets in our analysis. The
658 mutual event times are highly consistent across these data sets, though residual systematics in the
659 photometry result in slightly different event depths.
660

661 **Figure 4:**

662 **Observed mutual events of the Didymos system.** The data are marked as circles and the solid
663 curve represents the synthetic lightcurve for the best-fit post-impact solution. The dashed curve
664 is the pre-impact orbit prediction from ref.⁶. The primary and secondary events are shown on the
665 left and right sides of the plots, respectively. In some cases, the observations of a secondary
666 event precede those of a primary event (*i.e.*, their order in the data set is the inverse of that shown
667 in the plot). We present these events in reverse order and they are separated by a “//” symbol in
668 the plot (0.4728 day is to be subtracted from the x-coordinate of data points to the right from this
669

670 separator). The y-axis shows the magnitude on the night of the observation for each data set and
671 each tick mark has a range of 0.02 magnitudes.
672

673 **Extended Data Figure 1:**

674 **Goldstone radar echo power spectra.** Selected radar echo power spectra obtained at Goldstone
675 that were used to measure the Doppler separations in Table 6. The spectra were obtained in the
676 opposite sense of circular polarization as the transmitted wave. Each spectrum was integrated for
677 10-15 minutes in order to detect Dimorphos with minimum smear due to orbital motion (< 8
678 degrees). Echoes from Didymos are centered on 0 Hz and have a bandwidth of between 22-34
679 Hz. The echo from Dimorphos appears as a narrow spike superimposed on the signal from
680 Didymos, a pattern observed with radar observations of dozens of other near-Earth asteroids
681 (e.g.,⁴³), indicated by the arrows. The Doppler frequency of Dimorphos varies with time between
682 positive and negative values due to its orbital motion and estimated values can be found in Table
683 6. Dashed vertical lines show the Doppler frequencies of Dimorphos predicted by the pre-impact
684 orbit. Prediction uncertainties are smaller than the resolution of the spectra.
685

686 **Extended Data Table 1:**

687 **Pre-impact photometric observations.** Additional pre-impact photometric observations of
688 (65803) Didymos beyond those described in Pravec et al. (2022).
689

690 **Extended Data Table 2:**

691 **Post-impact photometric observations.** Post-impact photometric observations of (65803)
692 Didymos used to derive the new orbital period and period change as a result of impact.
693

694 **Extended Data Table 3:**

695 **Best-fit orbit parameters using the N22 method.** The input observations data is listed in
696 Tables 4, 5, 6, and 7. Note: Formal uncertainties are scaled by 2x in order to capture errors from
697 unmodeled sources.
698

699 **Extended Data Table 4:**

700 **Mutual event times measured in post-impact lightcurves for the N22+ approach.** All times
701 are one-way light-time corrected to reflect the time of the events at the asteroid, not the times
702 that they were observed from Earth. The beginnings and ends of events correspond to T_{1.5} and
703 T_{3.5}. The fourth column shows the post-fit residuals (observed - computed) for the solution in
704 Table 3, normalized by the 1-sigma uncertainty listed in the third column. The fifth column
705 shows the time since impact.
706

707 **Extended Data Table 5:**

708 **Goldstone radar range measurements of Dimorphos relative to Didymos.** The fourth column
709 shows the post-fit residuals (observed - computed) for the solution in Table 3, normalized by the
710 1-sigma uncertainty listed in the third column.
711

712 **Extended Data Table 6:**

713 **Goldstone radar Doppler measurements of Dimorphos relative to Didymos.** The fourth
714 column shows the post-fit residuals (observed - computed) for the solution in Table 3,
715 normalized by the 1-sigma uncertainty listed in the third column.

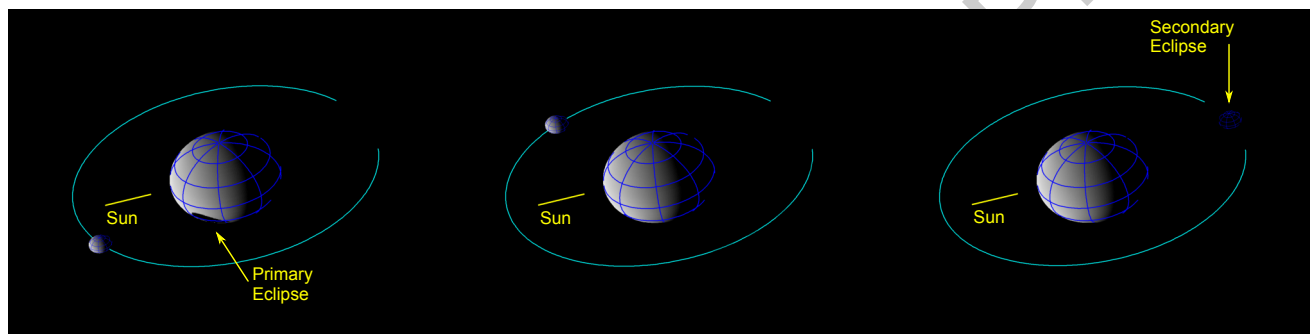
716

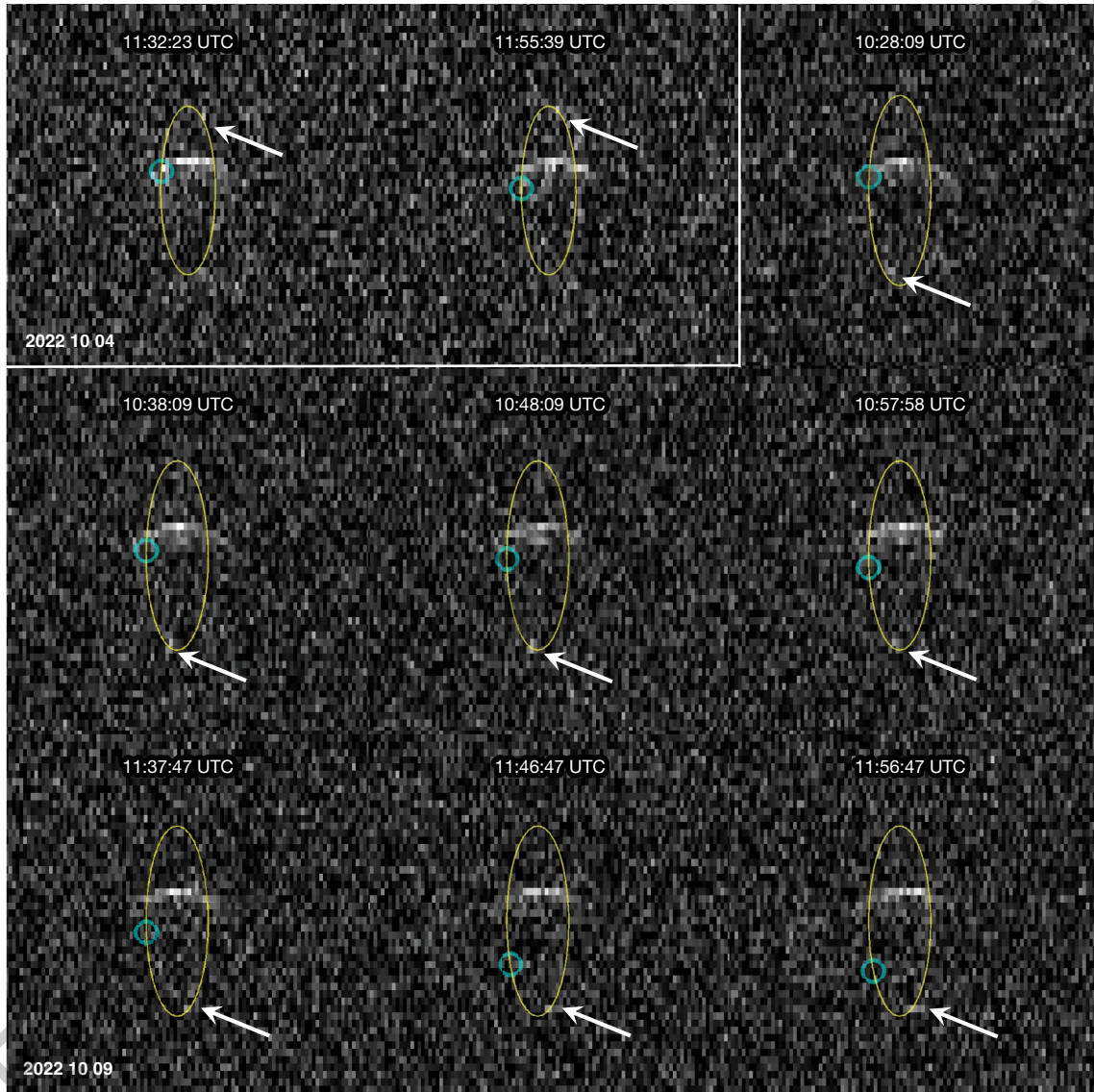
717

718 **Extended Data Table 7:**

Didymos-relative optical astrometry of Dimorphos.

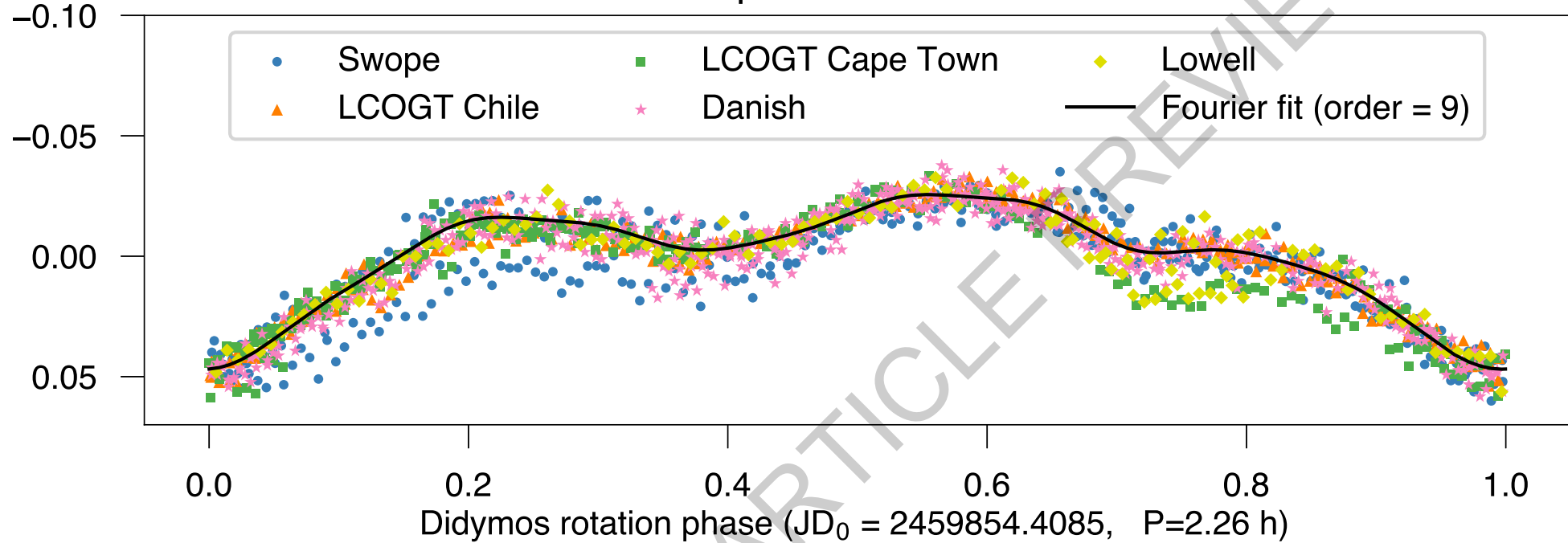
ACCELERATED ARTICLE PREVIEW



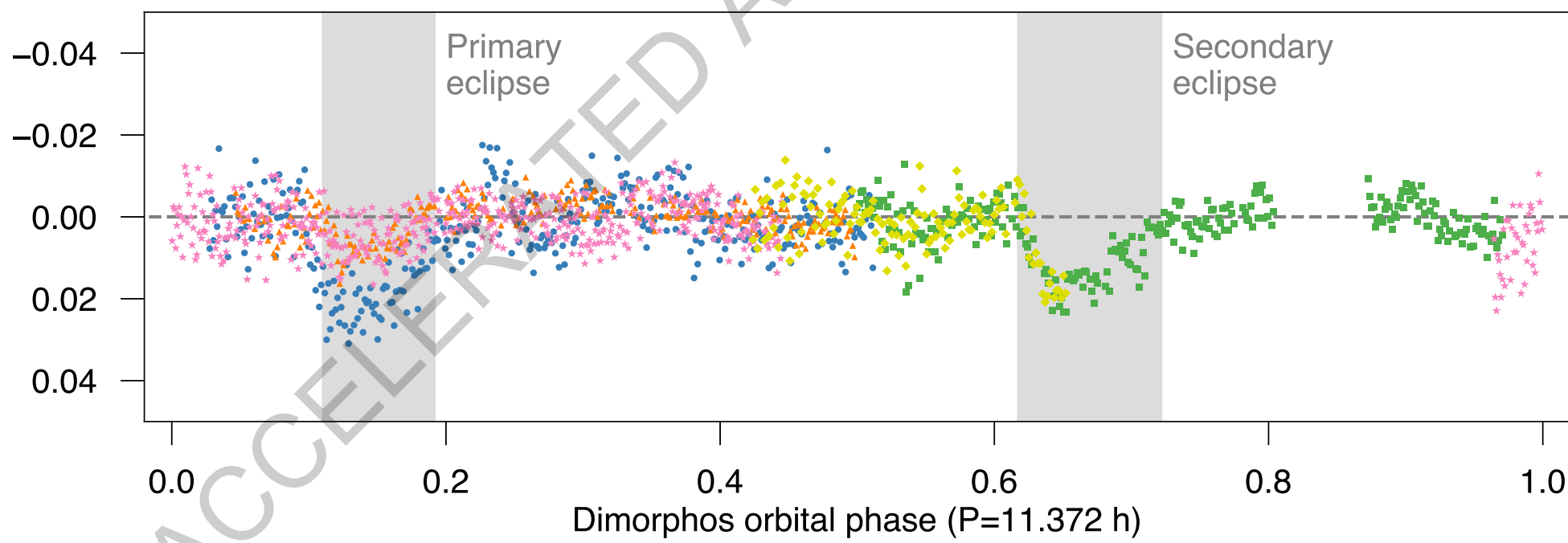


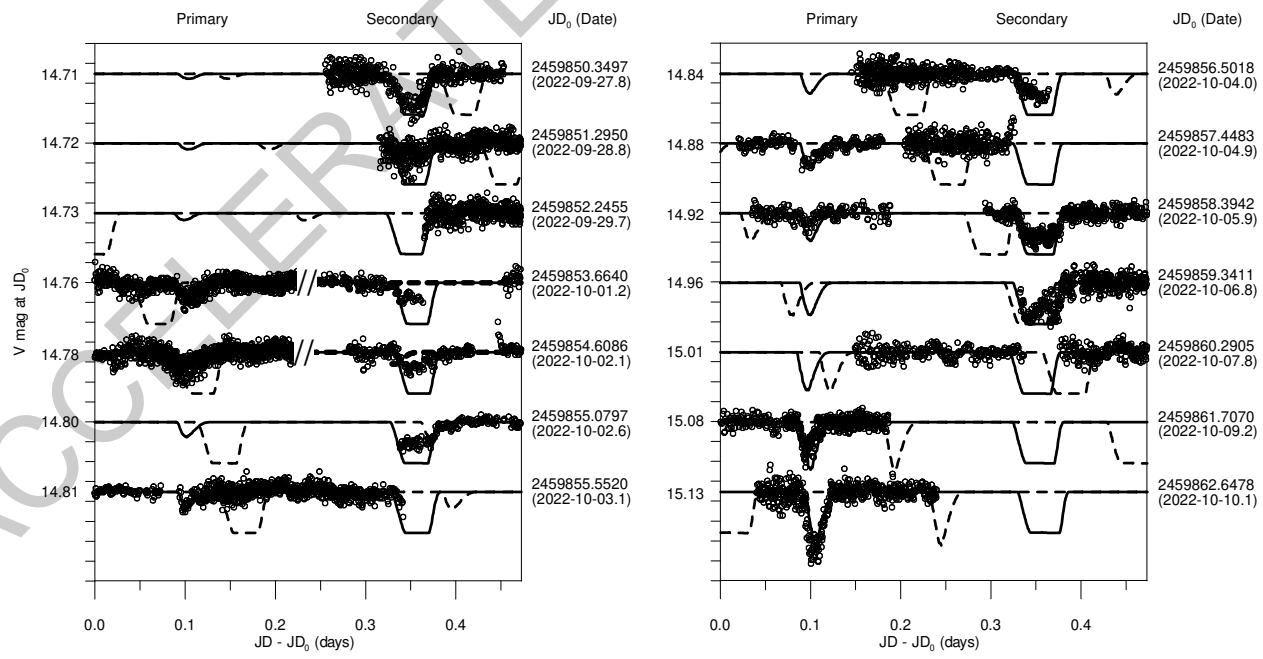
Post Impact: 2 October 2022

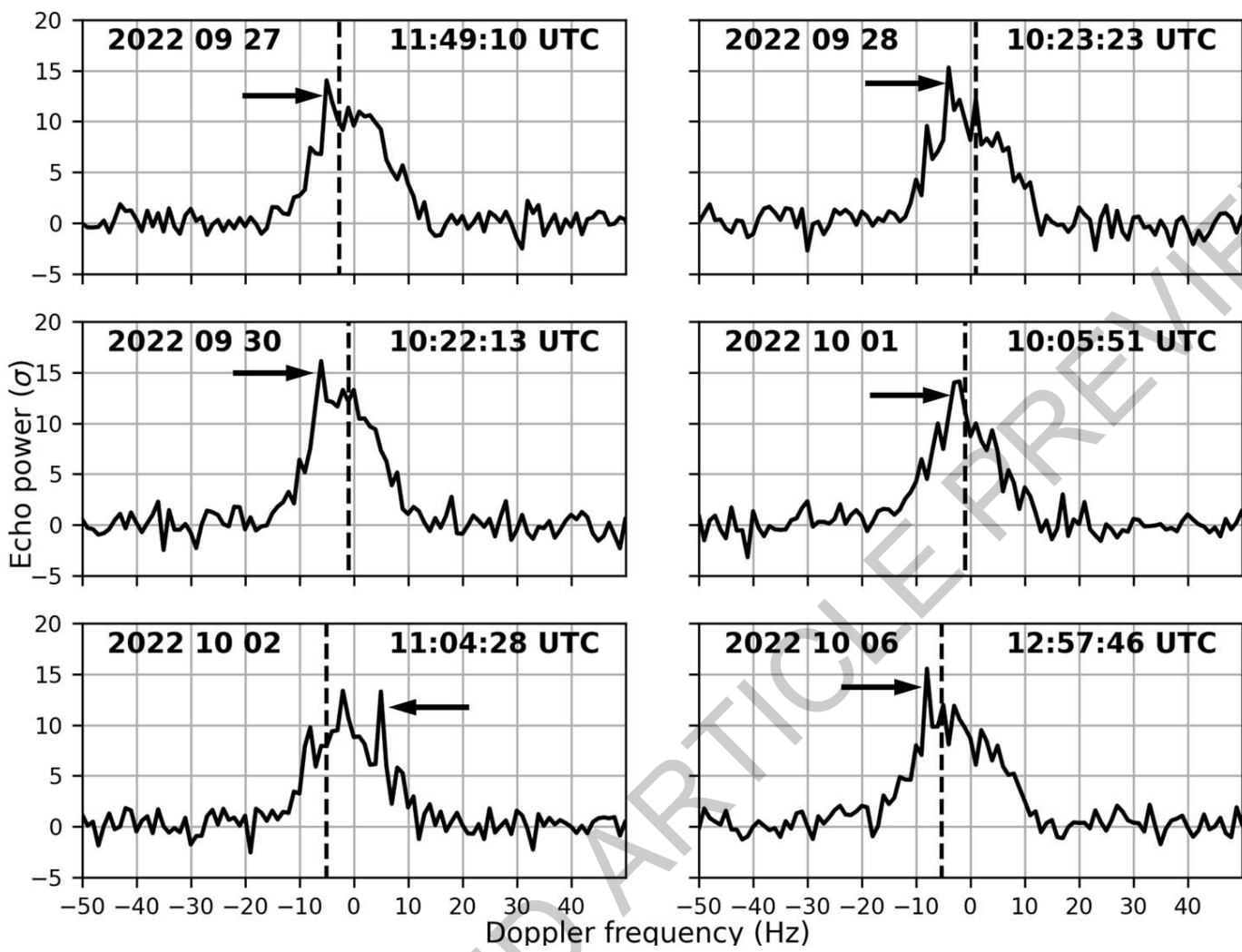
Differential Magnitude



Residual Magnitude







Extended Data Fig. 1

Date (UTC)	Start Time (UTC)	Duration (Hr)	# of Points	Telescope	RMS Residual (N22+) mag	RMS Residual (SP22) mag
2022-07-02	03:59	6.6	193	LCO/Magellan Baade 6.5-m	0.008	0.009
2022-07-04	06:52	3.8	129	CTIO/SOAR 4.1-m	0.007	0.006
2022-07-05	04:24	6.4	210	CTIO/SOAR 4.1-m	0.008	0.006
2022-07-06	08:02	3.2	89	Lowell Discovery Telescope 4.3-m	0.005	0.006
2022-07-07	07:50	3.5	85	Lowell Discovery Telescope 4.3-m	0.009	0.006

Extended Data Table 1

Date (UTC)	Start Time (UTC)	End Time (UTC)	Duration (Hr)	# of Points	Telescope	RMS Residual (N22+) mag	Slope Correction (N22+) mag/day	RMS Residual (SP22) mag	Slope Correction (SP22) mag/day
2022-09-28	2:33	6:09	3.6	237	LCO/Swope 1-m	0.008	0.10	0.008	0.07
2022-09-28	2:38	9:16	6.7	340	La Silla/Danish 1.54-m	0.006	0.10	0.006	0.12
2022-09-29	2:40	9:17	6.6	433	LCO/Swope 1-m	0.007	0.24	0.007	0.25
2022-09-29	2:50	9:33	6.7	639	La Silla/Danish 1.54-m	0.005	0.10	0.005	0.12
2022-09-29	4:52	8:47	3.9	212	CTIO/LCOGT-LSC 1-m	0.003	0.12	0.003	0.12
2022-09-30	2:40	9:41	7.0	669	La Silla/Danish 1.54-m	0.006	0.10	0.006	0.11
2022-09-30	2:52	9:15	6.4	420	LCO/Swope 1-m	0.008	0.20	0.008	0.20
2022-09-30	3:52	9:16	5.4	319	CTIO/LCOGT-LSC 1-m	0.004	0.12	0.004	0.12
2022-09-30	21:45	1:12	3.5	168	SAAO/LCOGT-CPT 1-m	0.004	0.22	0.004	0.21
2022-10-01	3:28	9:14	5.8	376	LCO/Swope 1-m	0.007	0.22	0.006	0.23
2022-10-01	4:00	9:11	5.2	292	CTIO/LCOGT-LSC 1-m	0.005	0.06	0.004	0.08
2022-10-01	6:33	9:28	2.9	278	La Silla/Danish 1.54-m	0.005	0.25	0.005	0.10
2022-10-01	21:48	3:09	5.4	268	SAAO/LCOGT-CPT 1-m	0.005	0.08	0.005	0.06
2022-10-02	3:05	8:33	5.5	530	La Silla/Danish 1.54-m	0.006	0.00	0.005	0.09
2022-10-02	3:15	9:19	6.1	359	LCO/Swope 1-m	0.007	0.15	0.006	0.16
2022-10-02	4:00	9:11	5.2	269	CTIO/LCOGT-LSC 1-m	0.004	0.02	0.003	0.00
2022-10-02	8:19	10:55	2.6	132	Lowell/Hall 1.1-m	0.005	0.15	0.006	0.09
2022-10-02	22:00	00:56	2.9	136	SAAO/LCOGT-CPT 1-m	0.003	0.00	0.003	0.00
2022-10-03	1:00	3:02	2.0	99	SAAO/LCOGT-CPT 1-m	0.003	0.10	0.003	0.13
2022-10-03	3:29	9:27	6.0	385	LCO/Swope 1-m	0.007	0.12	0.007	0.12
2022-10-03	4:05	8:42	4.6	248	CTIO/LCOGT-LSC 1-m	0.004	0.12	0.004	0.10
2022-10-03	4:27	5:28	1.0	98	La Silla/Danish 1.54-m	0.006	0.20	0.005	0.12
2022-10-04	3:46	8:24	4.6	224	LCO/Swope 1-m	0.006	0.15	0.006	0.11
2022-10-04	4:15	8:47	4.5	248	CTIO/LCOGT-LSC 1-m	0.005	0.05	0.005	0.04
2022-10-04	23:15	3:04	3.8	206	SAAO/LCOGT-CPT 1-m	0.005	0.00	0.004	0.00
2022-10-05	3:40	5:51	2.2	151	La Silla/Danish 1.54-m	0.006	0.10	0.006	0.00
2022-10-05	3:45	6:39	2.9	181	LCO/Swope 1-m	0.009	0.25	0.008	0.28
2022-10-05	22:18	1:59	3.7	194	SAAO/LCOGT-CPT 1-m	0.006	0.04	0.005	0.00
2022-10-06	3:49	9:20	5.5	346	LCO/Swope 1-m	0.010	0.06	0.009	0.06
2022-10-06	4:31	8:09	3.6	194	CTIO/LCOGT-LSC 1-m	0.005	0.10	0.004	0.10
2022-10-06	5:03	9:27	4.4	370	La Silla/Danish 1.54-m	0.005	0.00	0.005	0.14
2022-10-07	4:10	8:28	4.3	379	La Silla/Danish 1.54-m	0.006	0.12	0.006	0.11
2022-10-07	4:52	9:08	4.3	219	CTIO/LCOGT-LSC 1-m	0.007	0.10	0.007	0.09
2022-10-07	22:31	3:03	4.5	246	SAAO/LCOGT-CPT 1-m	0.007	0.05	0.006	0.05
2022-10-08	4:00	9:29	5.5	471	La Silla/Danish 1.54-m	0.007	0.15	0.006	0.06
2022-10-08	22:37	3:02	4.4	200	SAAO/LCOGT-CPT 1-m	0.010	0.05	0.011	0.00
2022-10-09	4:49	9:12	4.4	244	CTIO/LCOGT-LSC 1-m	0.006	0.00	0.005	0.00
2022-10-09	6:41	9:26	2.8	244	La Silla/Danish 1.54-m	0.007	0.00	0.005	0.06
2022-10-10	4:30	9:18	4.8	419	La Silla/Danish 1.54-m	0.006	0.12	0.006	0.06

Extended Data Table 2

Parameter	Estimate +/- 1σ uncertainties
Epoch (UTC)	2022 Sep 26 23:14:24.183
Orbit pole longitude (λ , degrees)	313.3 +/- 5.2
Orbit pole latitude (β , degrees)	-79.3 +/- 1.0
Pre-impact semimajor axis (a , km)	1.206 +/- 0.035
Mean anomaly at epoch (M_0 , degrees)	178.9 +/- 5.5
Pre-impact period (h)	11.921473 +/- 0.000044
Mean motion at epoch (n_0 , rad/sec)	(1.4640214 +/- 0.0000054) x 10^{-4}
Rate of change of mean motion (\dot{n} , rad/sec 2)	(5.4 +/- 1.6) x 10^{-18}
Post-impact period (h)	11.3712 +/- 0.0055
Period change (min)	-33.02 +/- 0.33
Change in mean motion (Δn , rad/sec)	(7.085 +/- 0.070) x 10^{-6}

Extended Data Table 3

Time (UTC)	Event type	Unc. (days)	Residuals (sigma)	Δt_{impact} (days)
2022 SEP 28 04:28:07	Beginning of secondary eclipse	0.011	0.50	1.22
2022 SEP 28 05:14:03	End of secondary eclipse	0.008	-0.94	1.25
2022 SEP 29 03:02:00	Beginning of secondary eclipse	0.01	-0.04	2.16
2022 SEP 29 03:39:53	End of secondary eclipse	0.0135	-1.45	2.18
2022 OCT 01 06:11:57	Beginning of primary eclipse	0.0075	0.58	4.29
2022 OCT 01 06:45:04	End of primary eclipse	0.008	0.71	4.31
2022 OCT 01 23:12:54	Beginning of secondary eclipse	0.0115	0.19	5.00
2022 OCT 02 00:08:03	End of secondary eclipse	0.0115	-0.55	5.04
2022 OCT 02 04:43:58	Beginning of primary eclipse	0.0075	-0.36	5.19
2022 OCT 02 05:28:45	End of primary eclipse	0.01	0.63	5.26
2022 OCT 02 22:57:47	End of secondary eclipse	0.0075	-0.23	5.99
2022 OCT 04 08:13:37	Beginning of secondary eclipse	0.01	1.23	7.37
2022 OCT 05 00:40:10	Beginning of primary eclipse	0.0085	-1.18	8.06
2022 OCT 05 01:22:30	End of primary eclipse	0.008	-0.50	8.09
2022 OCT 05 23:39:33	Beginning of primary eclipse	0.0045	0.40	9.02
2022 OCT 05 23:56:15	End of primary eclipse	0.0055	-1.89	9.03
2022 OCT 06 05:29:36	Beginning of secondary eclipse	0.005	1.23	9.26
2022 OCT 06 06:32:15	End of secondary eclipse	0.0055	0.17	9.30
2022 OCT 07 04:55:12	End of secondary eclipse	0.01	-1.30	10.24
2022 OCT 08 08:34:39	Beginning of primary eclipse	0.0065	1.28	11.39
2022 OCT 08 08:51:21	End of primary eclipse	0.007	-0.71	11.40
2022 OCT 09 07:12:25	Beginning of primary eclipse	0.0065	0.80	12.33
2022 OCT 09 07:33:35	End of primary eclipse	0.0085	-0.64	12.35
2022 OCT 10 05:54:48	Beginning of primary eclipse	0.005	1.06	13.28
2022 OCT 10 06:14:58	End of primary eclipse	0.0055	-1.19	13.29

Extended Data Table 4

Receive time (UTC)	Range (m)	Unc. (m)	Residuals (sigma)
2022 OCT 04 11:32:00	-825	150	-0.17
2022 OCT 04 11:55:00	-900	150	-0.36
2022 OCT 09 10:28:09	828	450	-0.14
2022 OCT 09 10:38:09	965	450	0.10
2022 OCT 09 10:48:09	942	450	0.00
2022 OCT 09 10:57:57	896	450	-0.13
2022 OCT 09 11:37:46	908	450	-0.03
2022 OCT 09 11:46:47	896	450	-0.00
2022 OCT 09 11:56:47	896	450	0.08
2022 OCT 09 12:05:46	862	450	0.08

Extended Data Table 5

Receive time (UTC)	Doppler (Hz)	Unc. (Hz)	Residuals (sigma)
2022 SEP 27 11:22:02	-3.00	2.00	0.12
2022 SEP 27 11:49:09	-5.00	2.00	-0.22
2022 SEP 28 10:23:24	-4.00	2.00	0.23
2022 SEP 30 10:22:13	-6.00	2.00	-0.32
2022 OCT 01 10:05:51	-2.50	2.00	-0.27
2022 OCT 02 11:04:28	5.00	2.00	-0.54
2022 OCT 04 09:58:15	7.00	2.00	-0.02
2022 OCT 06 12:44:16	-8.00	2.00	-0.18
2022 OCT 06 12:57:45	-8.00	2.00	-0.33
2022 OCT 12 09:37:43	8.00	2.00	-0.33
2022 OCT 12 10:26:49	9.00	2.00	0.20
2022 OCT 13 09:44:09	7.00	2.00	-0.27

Extended Data Table 6

Time (UTC)	ΔRA (deg)	ΔRA unc. (deg)	ΔRA residual (sigma)	ΔDEC (deg)	ΔDEC unc. (deg)	ΔDEC residual (sigma)
2022-09-26 23:10:58.235	-0.0514196	0.0038304	0.202	-0.0125218	0.0034673	0.08
2022-09-26 23:11:04.975	-0.0534928	0.0039585	0.12	-0.0117131	0.0034132	0.45
2022-09-26 23:11:11.715	-0.055801	0.0040724	0.016	-0.0125985	0.0034639	0.32
2022-09-26 23:11:18.456	-0.0576213	0.004194	0.067	-0.0134683	0.0035253	0.22
2022-09-26 23:11:24.233	-0.0593477	0.0043055	0.098	-0.0143021	0.0035859	0.11
2022-09-26 23:11:30.973	-0.0615916	0.0044643	0.115	-0.0140441	0.0035711	0.35
2022-09-26 23:11:37.713	-0.0641259	0.0046184	0.11	-0.0150902	0.0036472	0.23
2022-09-26 23:11:44.453	-0.0667637	0.0047804	0.127	-0.016572	0.003762	0.01
2022-09-26 23:11:51.193	-0.069919	0.0049938	0.087	-0.0157601	0.0036996	0.43
2022-09-26 23:11:57.933	-0.0732115	0.005196	0.076	-0.0170424	0.0038	0.29
2022-09-26 23:12:04.673	-0.0766707	0.0054239	0.093	-0.0180365	0.0038846	0.26
2022-09-26 23:12:11.413	-0.0803118	0.0056719	0.141	-0.019363	0.004004	0.17
2022-09-26 23:12:18.153	-0.0849044	0.0059557	0.094	-0.0204015	0.0040924	0.18
2022-09-26 23:12:24.893	-0.0893027	0.0062723	0.161	-0.0214126	0.0041959	0.22
2022-09-26 23:12:31.633	-0.0948127	0.0066306	0.14	-0.0225141	0.0042994	0.28
2022-09-26 23:12:39.336	-0.102054	0.0070766	0.105	-0.0253911	0.0045736	0.02

Extended Data Table 7